Palacký University Olomouc
Faculty of Science

Department of Optics

Design and trade-offs of digital holographic microscopy

Bachelor's Thesis

Rebeka Zrníková

Palacký University Olomouc
Faculty of Science

Department of Optics

Design and trade-offs of digital holographic microscopy

Bachelor's Thesis

Author:	Rebeka Zrníková
Study programme:	B0533A110011 Optics and Optoelectronics
Field of study:	1701R029 Optics and Optoelectronics
Form of study:	Full-time
Supervisor:	Mgr. Jaromír Běhal, Ph.D.
Co-Supervisor:	RNDr. Miroslav Ježek, Ph.D.

Thesis submitted on: 15 May 2024

Univerzita Palackého
Přírodovědecká fakulta

Katedra optiky

Principy a optimalizace digitální holografické mikroskopie

Bakalářská práce

Autor:	Rebeka Zrníková
Studijní program:	B0533A110011 Optika a optoelektronika
Studijní obor:	1701R029 Optika a optoelektronika
Forma studia:	Prezenční
Vedoucí:	Mgr. Jaromír Běhal, Ph.D.
Konzultant:	RNDr. Miroslav Ježek, Ph.D.

Práce odevzdána dne: 15. května 2024

Abstract

The Thesis is focused on the experimental implementation of digital holographic microscopy for live cell observation and the analysis of reconstructed images. Digital holographic microscopy is a non-invasive technique, which enables the acquisition of three-dimensional images of microscopic objects. The experimental setup, constructed as an off-axis digital holographic microscope, allowed us to capture interference recording of the sample with unstained cells on camera for subsequent reconstruction. The reconstruction process involved performing the Fourier transform on the captured image, extracting the necessary information from the Fourier domain, and then applying the inverse Fourier transform. By ensuring the precise alignment and characteristics of the optical components, three distinct diffraction orders were observable in the Fourier domain: the (0th) order, the (-1st) order, and the $(+1^{st})$ order. The quality of the reconstruction heavily relies on the size of the spectrum cut, which significantly influences the final resolution of the reconstructed image. We demonstrate the performance of the method by imaging human cheek cells. Furthermore, part of the Thesis also deals with the design of an advanced holographic microscope, where we aim for the best use of the imaging apparatus and the camera parameters in order to obtain the largest possible field of view with preserved optical resolution. This is done by setting the correct position and size of diffraction orders. The work will progress toward high-resolution three-dimensional reconstruction of live cells at the level of cell organelles in microfluidic systems.

i

Declaration

I hereby declare that I have written this Bachelor's Thesis—and performed all the presented research and experimental tasks—by myself, while being supervised by Mgr. Jaromír Běhal, Ph.D. and co-supervised by RNDr. Miroslav Ježek, Ph.D.. I also state that every resource used is properly cited. I agree with the Thesis being used for teaching purposes and being made available at the website of the Department of Optics.

Olomouc, 15 May 2024

REBEKA ZRNÍKOVÁ

Contents

Chapter 1

Introduction

Cell observation is a crucial aspect of research in various fields. It can aid in disease diagnosis, drug research, biotechnology development, and gaining a better understanding of the cellular level of the life process. This knowledge has the potential to make a significant impact on the treatment of diseases. Therefore, it is imperative to continuously improve technologies to enhance our ability to observe and study living cells with as much accuracy as possible.

However, common observations of cells from living organisms bring certain challenges. Nowadays, living cells are mainly observed using a light microscope. This type of microscopy is convenient, quick, and fully functional, but that does not mean it is perfect. The usefulness of direct light passage is limited due to insufficient contrast to resolve many parts of the cell [1], see Fig. 1.1 (a). In this case, the problem is solved by staining the cells with organic dyes [2], which increases contrast and visibility, see Fig. 1.1 (b). On the other hand, the staining process may kill the cells or irreversibly modify their structure. Moreover, cells

(a)	(b)
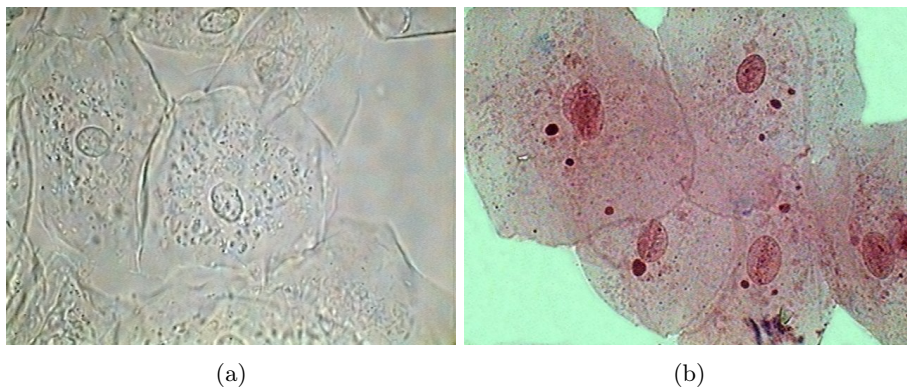
Figure 1.1: Comparison of stained and unstained cells. Panel (a) shows an example of unstained cheek cells. Panel (b) shows an example of cheek cells colored with 0.1% aqueous eosin. Adapted from [3].

in vivo often tend to move in the sample, which makes it difficult to observe them and focus on specific parts of the sample. This is a problem for which a solution has been found in the form of specimen fixation interfering with its internal

structure. When attempting to capture images of moving cells, the resulting images may not be of the desired quality due to blurring caused by the cell movement. In the case of living cells, it is also important to define a time window during which they are suitable for observation, the properties of the cell remain unchanged. The above-noted reasons highlight the importance of introducing new ways for observing cells that do not alter their internal structure, are fast, and provide the required resolution. Indeed, several methods evolved, including techniques for single-shot quantitative phase imaging. These techniques could provide the best way how to deal with these challenges. The development of phase microscopy has progressed over the years, and currently, there are several established techniques for its implementation. Phase microscopy can be divided into qualitative and quantitative approaches.

The main representative of qualitative phase microscopy is the Zernike technique, which was used, for example, in [4], where it was implemented in scanning X-ray microscopy to image the structural details of a sample. Experimental results confirmed that Zernike phase contrast is effective in visualizing structural information in biological samples with minimal impact on quantitative mapping of trace elements. Another technique is differential interference contrast, which was utilized in [5], where the authors observed the detailed structures and dynamics of living biological cells, using the Vorticella protist as a model organism.

Quantitative phase microscopy can be further divided into interferometric and non-interferometric methods. Non-interferometric methods include the transport of intensity equation, which is described in more detail in [6, 7, 8], as well as iterative algorithms, for example, in [9, 10]. On the other hand, interferometric methods consist of holography and interferometry. The main difference is that holography records complete optical information about an object to create a three-dimensional reconstruct [11], whereas interferometry uses the interference pattern between two light beams for quantitative measurements [12]. Holography can then be combined with interferometry to create holographic interferometry [13].

In this Thesis, we will look at the use of digital holographic microscopy for live cell observation, given that it is a non-invasive technique that allows real-time imaging of live cells without the need for staining or fixation. The first experiment of digital holographic microscopy for cell observation was carried out in 1990s by Schnars and Jueptner, who used a CCD camera directly connected to a computer [14]. Ever since then, the ways of observation have been improving.

In Chapter 2 we will discuss the basic theory behind digital holographic microscopy, introducing the Fourier transform of an image and two elementary types for 3D imaging. Chapter 3 focuses on the experimental implementation, where is also discussed the process of the complex-amplitude reconstruction. Chapter 4 is dedicated to the discussion of experimental trade-offs, where we also discuss the dependence of the resolution and the noise on the size of the spectrum cut. In Chapter 5 we will look into the design of advanced holographic microscopy, where we focus on finding the ideal configuration of the diffraction orders. Finally, the results are summarized in Chapter 6. We also describe possible future research directions.

Chapter 2

Digital holographic microscopy

Digital holographic microscopy is an innovative technique merging the principles of digital holography with the precision of microscopic examination which allows the meticulous quantitative three-dimensional analysis of microscopic objects with high resolution and contrast, revolutionizing the field of microscopic analysis.

The concept of holography was first proposed in 1947 by scientist Dennis Gabor, leading to the development of the first three-dimensional holographic image using a laser in the early 1960s by Emmett Leith and Juris Upatnieks [15, 16]. Holography is a way of obtaining a three-dimensional record of an object [17]. It allows reconstruction of the complex amplitude of light interacting with the sample [18]. This means that the process of hologram formation exploits a mixture of at least two coherent light waves that are superposed [19]. The hologram plane may receive light either reflected from the object or transmitted through it. This wave is called the object wave U_0. At the same time, the plane of the hologram is illuminated by another light wave, referred to as the reference wave U_R [20]. Hence, the waves with complex amplitudes U_R and U_O are superposed and give the resulting intensity

$$I = |U_R + U_O|^2 = |U_R|^2 + |U_O|^2 + U_R^* U_O + U_R U_O^*. \tag{2.1}$$

This equation for intensity is composed of three important parts. The two terms $|U_R|^2$ and $|U_O|^2$ are referred to as the zero-order terms. The next two terms are mutually complex conjugated. The term $U_R^* U_O$ is referred to as the $(+1^{st})$ order and the term $U_R U_O^*$ is referred to as the (-1st) order [21]. In the case of digital holography, the recording process exploits a pixel matrix sensor, such as a CCD or CMOS camera, to capture the interference record (2.1) [20].

In the Fourier transform, an arbitrary function $f(x, y)$ is decomposed into a series of harmonic functions with different spatial frequencies (number of cycles per unit length) and complex amplitudes. The two-dimensional Fourier transform can be determined as

$$F(\nu_x, \nu_y) = \int_{-\infty}^{\infty} \int_{-\infty}^{\infty} f(x, y) \exp[-i2\pi(x\nu_x + y\nu_y)]\mathrm{d}x\mathrm{d}y, \tag{2.2}$$

where ν_x and ν_y are spatial frequencies in given x and y axes. Consequently, the inverse Fourier transform will be

$$f(x,y) = \int_{-\infty}^{\infty}\int_{-\infty}^{\infty} F(\nu_x, \nu_y) \exp[i2\pi(x\nu_x + y\nu_y)]\mathrm{d}\nu_x\mathrm{d}\nu_y \qquad (2.3)$$

This means that signal $f(x,y)$ can be expressed as the sum of weighted plane waves. To obtain information about the period of the interference fringes at a given tilt, a monochromatic plane wave with complex amplitude $U(x,y) = A\exp\left[-i(xk_x + yk_y)\right]$ is considered, where A represents the amplitude and $\vec{k}$ is the wavevector with components $\vec{k} = (k_x, k_y)$. This wave must interfere with the collinear wave (perpendicular to the x-y plane) as we need at least 2 waves for interference. The wavenumber can be determined as $k = \frac{2\pi}{\lambda}$ and the angle it makes with the $x - y$ plane as $\cos(\theta_x) = \frac{k_x}{k}$. Using spatial frequency $\nu_x = \frac{k_x}{2\pi}$, it can be modified as

$$\cos(\theta_x) = \lambda\nu_x, \qquad (2.4)$$

where λ is the wavelength. Given the fact that the period is the inverse of the spatial frequency, it will be expressed as

$$\Lambda = \frac{\lambda}{\cos(\theta_x)} \qquad (2.5)$$

[22].

The Fourier transform of the image produces a Fourier spectrum, the resolution of which is largely influenced by the properties of the camera. Namely, the pixel size in the Fourier domain in the x-axis and y-axis direction follows

$$\Delta f_{\mathrm{x}} = \frac{1}{\mathrm{M_x}\Delta x}, \qquad (2.6)$$

where Δf_{x} is the spatial spectrum resolution in the x-direction, M is the number of camera pixels in the horizontal direction, Δx is the width of one pixel, and

$$\Delta f_{\mathrm{y}} = \frac{1}{\mathrm{M_y}\Delta y}, \qquad (2.7)$$

where Δf_{y} is the spatial spectrum resolution in the y direction, N is the number of camera pixels in the vertical direction, and Δy is the height of one pixel.

If a coordinate system is suitably chosen with the origin located at the center of the spectrum, the size of the Fourier domain is determined by the maximum spatial frequency, which in the x-direction is given by

$$f_{\mathrm{x,max}} = \frac{1}{\mathrm{M_x}\Delta x}\frac{\mathrm{M_x}}{2} = \frac{1}{2\Delta x}, \qquad (2.8)$$

and in the y-direction

$$f_{\mathrm{y,max}} = \frac{1}{\mathrm{M_y}\Delta y}\frac{\mathrm{M_y}}{2} = \frac{1}{2\Delta y}. \qquad (2.9)$$

The maximum spatial frequency of the resulting spectrum for square pixels (Δx=Δy) is the same either in the x-axis or in the y-axis, although with different sampling if $\mathrm{M_x} \neq \mathrm{M_y}$. This follows from the Nyquist-Shannon sampling

theorem, which states that a sampling twice as dense as the minimum period (the inverse of the frequency) is necessary. Any higher frequency will appear the same as some lower ones [22].

Holography is classified into two elementary types for 3D imaging, which are Gabor´s holography, with the use of in-line holography, and Leith and Upatnieks' holography, where they used off-axis holography. This division is often based on the angle between the object and reference waves [21].

2.1 In-line digital holography

In in-line holography, there is usually no significant tilt between reference and object wave [19]. The obtained interference record has the form (2.1). Still, after performing the Fourier transform to plot the spectrum with the diffraction orders, they are found to overlap each other, see Fig. 2.1 (a). The interference intensity (2.1) can also be written as

$$I = |U_\mathrm{R} + U_\mathrm{O}|^2 = |U_\mathrm{R}|^2 + |U_\mathrm{O}|^2 + 2U_\mathrm{R}U_\mathrm{O}\cos[\varphi + \psi], \qquad (2.10)$$

where the ψ represents the phase shift and $\varphi = \varphi_\mathrm{R} - \varphi_\mathrm{O}$ the phase change of the interfering waves. To separate the contributions of interfering waves, one of the waves (usually the reference wave) can be modulated independently. Initially, a record is made where the wave is not shifted in phase. Then, additional snapshots with various mutual phase shifts are recorded. Usually, a four-step phase-shifting algorithm, with phase shifts $\psi = 0, \frac{\pi}{2}, \pi, \frac{3\pi}{2}$ is implemented. The acquired interference records have the following form

$$I_1 = |U_\mathrm{R}|^2 + |U_\mathrm{O}|^2 + 2U_\mathrm{R}U_\mathrm{O}\cos\varphi \qquad (2.11)$$

$$I_2 = |U_\mathrm{R}|^2 + |U_\mathrm{O}|^2 - 2U_\mathrm{R}U_\mathrm{O}\sin\varphi \qquad (2.12)$$

$$I_3 = |U_\mathrm{R}|^2 + |U_\mathrm{O}|^2 - 2U_\mathrm{R}U_\mathrm{O}\cos\varphi \qquad (2.13)$$

$$I_4 = |U_\mathrm{R}|^2 + |U_\mathrm{O}|^2 + 2U_\mathrm{R}U_\mathrm{O}\sin\varphi. \qquad (2.14)$$

Consequently, the resulting phase of the interference record can be obtained as

$$\varphi = \arctan\Big[\frac{I_4 - I_2}{I_1 - I_3}\Big] \qquad (2.15)$$

[23]. However, this indicates that multiple images must be recorded, so its use is more likely to be associated with static samples.

2.2 Off-axis digital holography

Digital holography is called off-axis if there is a slight tilt between the two waves, the reference wave is tilted, and when they are separated [19]. The obtained interference record has again the form shown in (2.1) and in this case, the Fourier spectrum shows three separate orders, $(+1^{st})$ order, (-1st) order, and the zero-order, see Fig. 2.1 (b). The angle between the object and reference beams allows the various real and virtual image terms to be spatially separated, avoiding the problem of in-line holography. By numerically filtering the $(+1^{st})$ order in the Fourier domain, the complex amplitude of the object beam can be

reconstructed. This involves shifting the $(+1^{st})$ order to the zero frequency and taking the inverse Fourier transform. This process is described in more detail in Chapter 3. This type of holography is used to observe moving samples due to the fact that a single image is sufficient for correct reconstruction.
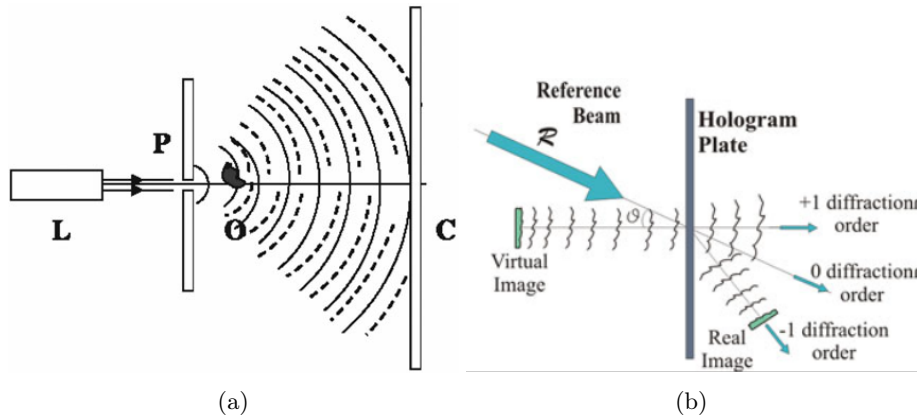

Figure 2.1: Panel (a) shows a schematic view of in-line digital holography, while panel (b) shows a schematic view of off-axis digital holography. Adapted from [24].

Chapter 3

Experimental implementation

3.1 Experimental setup and its description

The experimental setup of a simple digital holographic microscope is shown in Fig. 3.1, where a Helium-Neon laser with the wavelength $\lambda = 633$ nm was used as the light source. The emitted laser beam was directed to the mirror and then
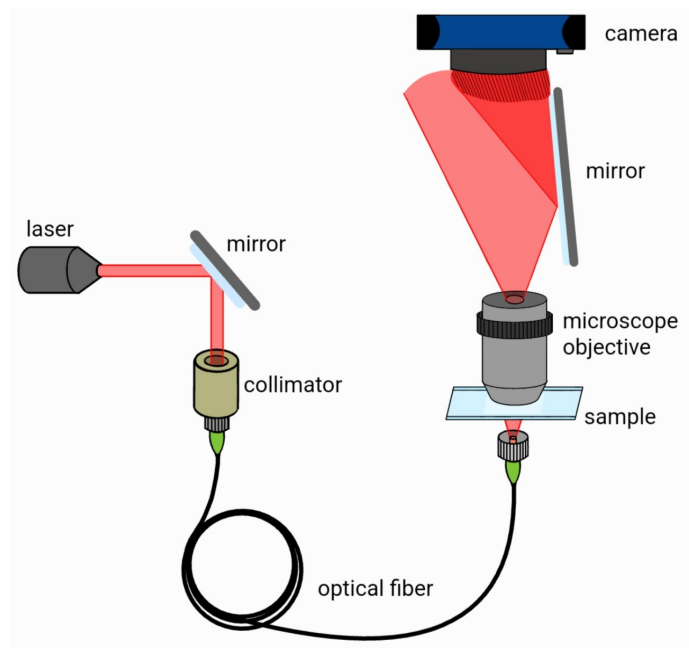

Figure 3.1: Sketch of the used digital holography microscope.

the beam was focused by a collimator and coupled into a single-mode optical fiber (FC/APC). The light emitted from the optical fiber directly illuminated the sample, which was placed on a three-dimensional translation stage. This stage allowed precise manipulation of the sample, which was convenient for focusing and finding a suitable sample location. An Olympus microscope objective (20x, NA=0.4) was used for imaging the sample on the camera (DMK 23U274). The

image acquisition and data storage were performed using a camera connected to a computer.
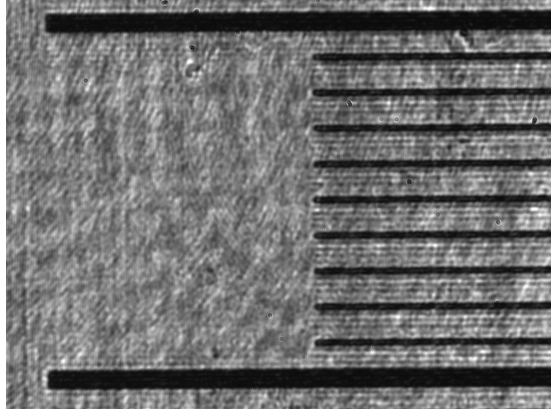

Figure 3.2: Camera recording of a scale with two larger bars spaced $100\,\mu\mathrm{m}$ apart.

In the proposed experiment, the transverse magnification was determined by the ratio of the image size m' to the object size m

$$\beta = \frac{m'}{m}. \qquad (3.1)$$

This was done by placing an object of known parameters (line target with $100\,\mu\mathrm{m}$ spacing), which was imaged, see Fig. 3.2, and the image size was obtained from known parameters of the used camera. Consequently, the established transverse magnification reached 46x.

An additional mirror was placed into the optical path between the microscope objective and the camera. The mirror reflected a sample-free portion of light transmitted via microscope objective. Hence, an off-axis geometry was created by reflecting a part of the object beam on itself. Consequently, interference fringes appeared on the camera record. The ratio of distances between the microscope objective, camera, and additional mirror in the experimental setup sketched on the Fig. 3.1 does not correspond to reality but serves for illustration purposes. The key components are listed in Table 3.1.

Moreover, cheek cells were chosen as the sample. A drop of water was put on a microscope slide. Using a wooden stick, a cheek swab was performed to obtain the cells that were smeared into the water on the microscope slide. They were then covered with a coverslip and placed into the object plane of the microscope objective.
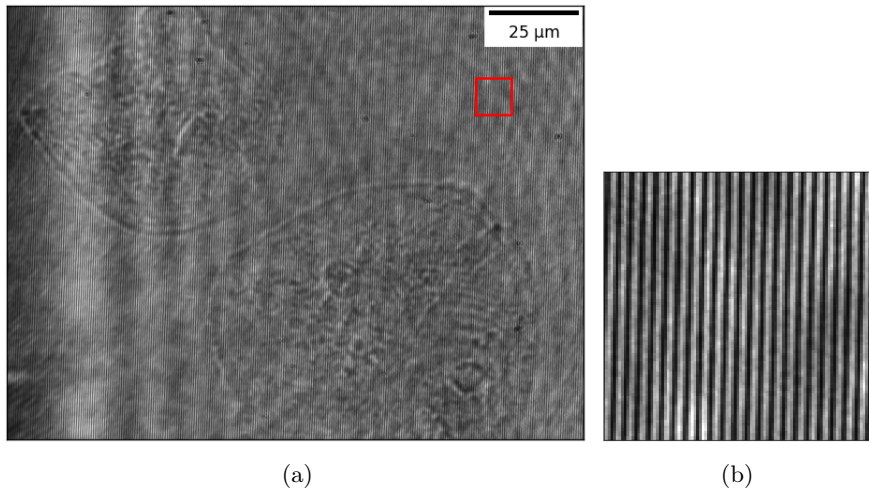
Figure 3.3: Panel (a) shows an example of a recorded interference pattern obtained using the built digital holographic microscope with cheek cells used as a sample. Panel (b) is a zoom-in of the recording with clearly visible interference fringes. The zoom-in was taken from the location of the red square in panel (a).

Table 3.1: The Key components used in experimental setup.

Component	Type	Relevant information
Light Source	He-Ne laser	Wavelength: 633 nm
Optical fiber	405-HP	Connector: FC/APC
Microscope objective	Olympus PLN 20X	Numerical aperture: 0.4
Camera	DMK 23U274	Number of pixels: 1600x1200
		Size of pixels: 4.4 µm
Output collimator	60FC-4-M8-33	AR-Coating: 390 - 670 nm

3.2   The complex-amplitude reconstruction

The captured camera recording in Fig. 3.3 (a) has the form of interference fringes, which arise due to the interference of light waves (2.1). Therefore, the required phase information must be retrieved numerically to get the valuable information. The Python programming language was used for this processing, specifically the interactive development environment JupyterLab and libraries numpy, scipy, mathplotlib, cv2. The first step to get the record reconstruction was to perform the Fourier transform of the acquired record. The Fourier transform provides the mapping of the image into the frequency domain. This yields a Fourier spectrum of spatial frequencies.

After the Fourier transform, an analysis of the Fourier spectrum was conducted shown in Fig. 3.4. The parameters of the used camera determine the sampling of the spectrum (2.6) - (2.9). In the spectrum three separated diffraction orders are formed for our experimental configuration. For the next reconstruction step, only the part of the spectrum that contains the wanted complex

amplitude is needed. This information is contained in the highlighted diffraction
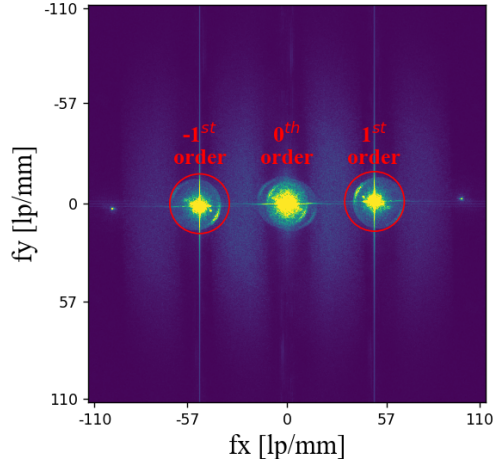

Figure 3.4: The absolute value of the Fourier transform of the camera recording. The image is saturated for better visibility of diffraction orders. lp means line pairs. This is the spectrum in the image plane, that is, in the plane where the camera is placed.

orders, thus the next necessary step is to cut out the Fourier spectrum of the spatial frequencies.

The size of the spectram cut is given by the maximum spatial frequency transmitted by a coherent imaging system, which is given in the object space as

$$\nu_{\max} = \frac{\text{NA}}{\lambda}, \tag{3.2}$$

where NA is the numerical aperture of the microscope objective and λ is the wavelength of the used light. In many cases, it is useful, to make evaluations in both, the object space and the image space, respectively. The transition between both spaces is realized via lateral magnification β (3.1). Consequently, the maximum transmitted spatial frequency in the image space takes an approximate form

$$\nu'_{\max} = \frac{\text{NA}}{\lambda\beta} = \frac{\nu_{\max}}{\beta}. \tag{3.3}$$

By calculating this spatial transmitted frequency, a theoretical optimum was obtained for the size of the spectrum cut around one of the highlighted diffraction orders. The next step was an inverse Fourier transform of the cut part of the spectrum, after which a complex amplitude was obtained. The retrieved phase is present in Fig. 3.5 (a).

Furthermore, reference recordings were made in cell-free regions. These are locations close to the originally observed cell. The reconstruction of this reference interference pattern followed an identical procedure as the record with the cheek cell. The phase change can be displayed in Fig. 3.5 (b).

There is a visible phase background in the images shown in Fig. 3.5 which may impair the quantitative analysis and would therefore be useful to correct for. The reconstructed complex amplitudes were taken for phase correction,
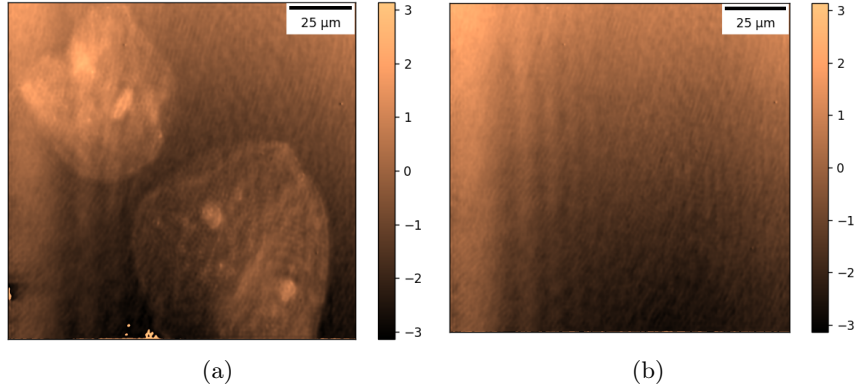
Figure 3.5: Panel (a) shows the phase reconstruction of cheek cells. Panel (b) shows the phase reconstruction of cell-free area.

then divided and the phase was made from the result of their division. This is how the final reconstruction is obtained where only the cell without background influence can be observed. Using this process, the absolute value of the complex amplitude was also displayed for comparison, from which it can be estimated that the phase reconstruction offers a more contrasting view of the cells, see Fig. 3.6.
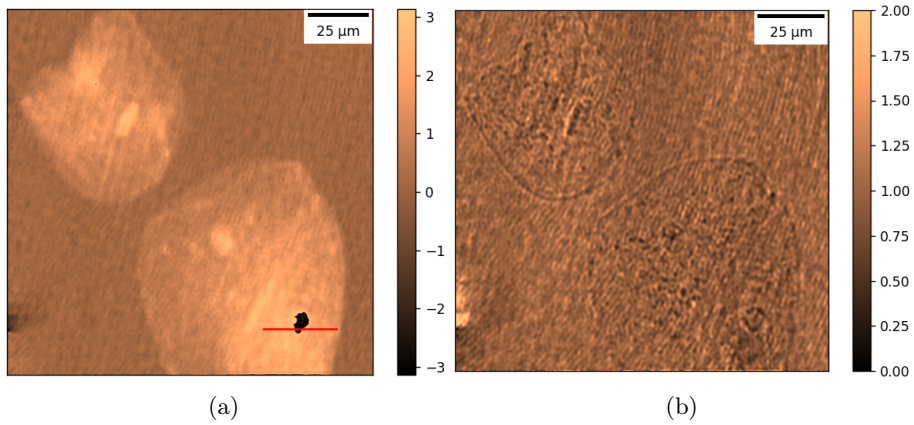

Figure 3.6: Panel (a) shows the final phase reconstruction of a sample with cheek cells. Panel (b) shows the absolute value of the complex amplitude of a sample with cheek cells.

The dark spot in one of the observed cells, see Fig. 3.6 (a), represents a phase jump. In reality, the observed cell should have a smooth phase profile, hence with the increasing measured optical path difference also the value of the reconstructed phase should increase. However, a numerically retrieved phase is limited from $-\pi$ to π as the direct phase detection on the use of arctangent operation for phase calculation. In the position, where the profile exceeds π, there was an inherent jump to $-\pi$, where it resumed growing again. This jump occurred due to the physical properties of the sample. In the case of cheek cells,

11

this often occurs especially in the place where the nucleus is located, which has the largest refractive index and therefore the largest phase delay is induced. A solution to this problem is the use of the process called phase unwrapping [24], example of which is shown in Fig. 3.7.
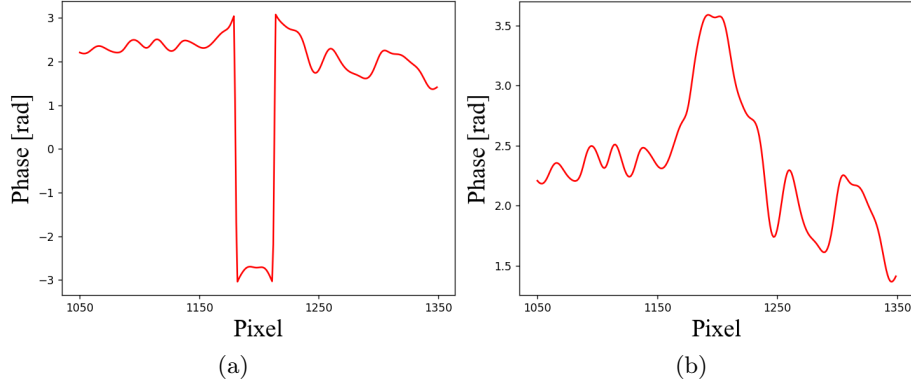

Figure 3.7: Panel (a) shows phase progression with a jump in the area of the black spot from the reconstruction in Fig. 3.6 (a). Panel (b) shows the unwrapped phase progression.

The result of the phase-correction process provides a realistic idea about the optical path difference induced by cells at particular locations in the sample. The following relationship is used for this calculation

$$\Delta\varphi = \frac{2\pi}{\lambda} \cdot \Delta n \cdot d, \tag{3.4}$$

where $\Delta\varphi$ is the phase change, λ is the wavelength, Δn is the change of refractive index and d is the thickness. We can then use the collected information to show the optical path difference $\Delta n \cdot d$, see Fig. 3.8.
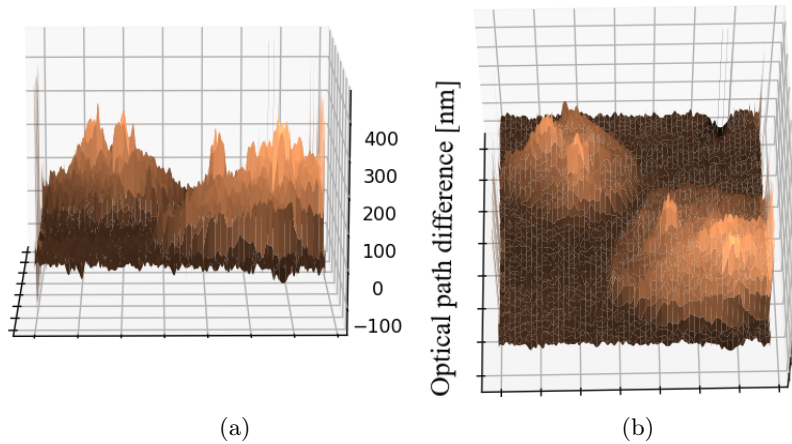
Figure 3.8: Optical path difference of cheek cells shown in 3D model from different angles.

By monitoring the change in cell optical path difference, it is possible to get a better insight into the internal structure of the cell and, for example, determine the location of the nucleus when studying it. It is expected that the cell will have the greatest phase delay here. It is worth noting, that this cell observation using off-axis holographic microscopy was carried out without the need for staining with chemicals or invasive modifications of their internal structure.

Chapter 4

Discussion of experimental trade-offs

Appropriate choice of experimental arrangement is crucial for correct high-resolution complex-amplitude retrieval. Each component in the experimental setup (sketched in Fig. 3.1) impacts the quality of the final reconstruction due to the non-trivial relation between optical parameters and holographic imaging performance, as will be discussed below.

4.1 The influence of experimental components

As mentioned in the description of the experiment a Helium-Neon laser with a wavelength of 633 nm was used. Initially, the maximum transmitted spatial frequency (3.3) is inverse, proportional to wavelength. It means that the maximum transmitted spatial frequency increases with decreasing wavelength. Another example is the period of the interference fringes produced by the interference of the reference and object waves, which is given by (2.5). Hence, a longer illumination wavelength increases the period of interference fringes and consequently positions of the diffraction orders in the Fourier spectrum. The larger the period, the closer together the diffraction orders are, and vice versa.

The next component is the microscope objective, where attention must be paid to the value of its numerical aperture and magnification. It is worth noting that the magnification indicated on the microscope objective refers to the specific tube lens. For the OLYMPUS objective used in the experiment (20x), it is a tube lens with a focal length of 180 mm, and according to the equation for lateral magnification

$$\Gamma = \frac{f_{\mathrm{TL}}}{f_{\mathrm{MO}}}, \tag{4.1}$$

the focal length of the microscope objective is 9 mm. As already shown the numerical aperture of the microscope objective occurs at the maximum transmitted spatial frequency (3.3). With a larger numerical aperture, this frequency is also larger. The change in magnification obtained by the constructed holographic microscope after performing the Fourier transformation would affect the appearance of the produced diffraction orders, specifically in their magnitude. Smaller lateral magnification generates larger diffraction orders in the

spectrum, which is also evident from the relation for the maximum transmitted spatial frequency in the image space, see Eq. (3.3).

The position of the mirror placed between the microscope objective and the camera also determines the appearance of the interference fringes. Its positioning allows setting the angle between the interfering waves, leading to different geometry of the spectra, as shown in Fig. 4.1. From the relation (2.5), it is concluded that the larger the cosine of the angle between the waves the smaller the period is.
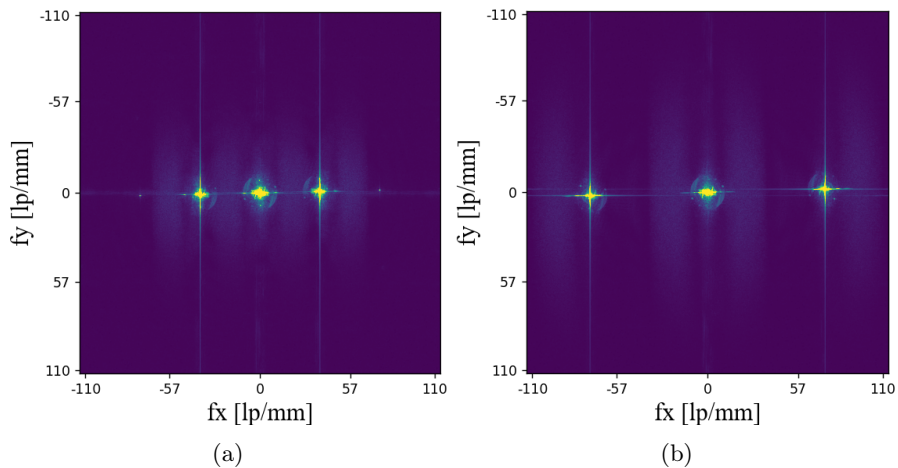

Figure 4.1: The influence of the mirror on the geometry of the Fourier spectrum. In panel (b) the mirror was placed 7.5 cm closer to the microscope objective, than in panel (a). The period of interference fringes has decreased and diffraction orders shifted further apart. The spectrum is in the image plane.

By shifting and tilting this mirror the period of the interference fringes can be conveniently adjusted. Optimally, all three diffraction orders should be visible in the resulting spectrum without mutual overlap. Fig. 4.1 (a) and Fig. 4.1 (b) represent examples from initial calibration measurements taken from different mirror positions relative to the microscope objective. In the final experiments, the interference fringes were adjusted as is sketched in Fig. 3.3 and the corresponding spectrum is shown in Fig. 3.4.

The last key component was the camera, whose features consist of the number and size of pixels. These properties influence the range and sampling in the Fourier domain. Relations (2.6) and (2.7) show that for smaller pixel counts, the pixel size in the Fourier domain will be larger. The smaller the size of the camera pixels, the larger the pixel size in the Fourier domain. On the other hand, the maximum frequency, whether in the x or y axis direction, depends only on the pixel size, so as the pixel size decreases, the maximum sampling frequency increases.

It is important to put all these parameters and trade-offs in context to obtain a record suitable for further reconstruction, but it is also necessary to be careful how we proceed with the numerical processing because the final form of the phase reconstruction can be influenced during the processing of the record, not only during the execution of the experiment.

4.2   The parameters of the phase reconstruction

During the reconstruction process of the camera interference record, a circular cut is made around one of the diffraction orders in Fig. 3.4. The inverse Fourier transform is performed only from this cut part. Whether we take the left (-1) or the right (+1) diffraction order does not matter, given that both contain the same information, as can be seen from the interference law (2.1). However, the magnitude of this cut will clearly affect the resulting reconstruction. Considering a small cut of a diffraction order is taken from the spectrum (a small portion near the center of that diffraction order) only the low spatial frequencies are selected, which represent contributions of harmonic functions with long periods. This choice results in a loss of sharpness, detail, and resolution after performing the inverse Fourier transform. On the other hand, when a large cut of a diffraction order is taken from the spectrum, the reconstruction suffers from increased noise originating from redundant information. In the previous chapter, it was stated that the magnitude of the cut is determined by the maximum transmitted spatial frequency (3.3). This frequency determines the optimal theoretical radius of the circular cut in the Fourier domain. This radius should determine the size of the cut, which will contain information about the sample details but will not take useless information.

In Fig. 4.2 (a) the spectrum cut of the diffraction order was 4 times smaller than the theoretical limit (3.3). Fig. 4.2 (b) shows the horizontal section of this reconstruction, where we can see smooth phase progression. For the reconstruction shown in Fig. 4.2 (c), there was used the calculated cut given by the theoretical limit (3.3). From the horizontal section in Fig. 4.2 (d), it is visible the increase of the noise in comparison with the phase shown in Fig. 4.2 (b). The last reconstruction was done by having the cut 2 times bigger than the magnitude of a cut calculated using the formula (3.3) and can be seen in Fig. 4.2 (e), with its horizontal section shown in Fig. 4.2 (f). It is visible that in the Fig. 4.2 (a), where the cut was small and the higher space frequencies were lost, the reconstruction lost sharp edges. On the other hand, if we took a closer look at the Fig. 4.2 (e), it provides the increase in phase variability. It can be seen from the horizontal sections that as the cutoff radius increases, fluctuations in reconstruction increase as well. The Fig. 4.2 (c) is supposed to represent the reconstruction based on the optimal cut given by (3.3). However, this is a theoretical optimum and, therefore, an additional experimental analysis was performed.

This analysis served to determine the exact optimum size of the spectrum cut for the constructed experiment and provided experimental confirmation of the theoretical value. Further analysis was carried out using just the displayed horizontal sections, from which information about the resolution and additional noise was obtained.
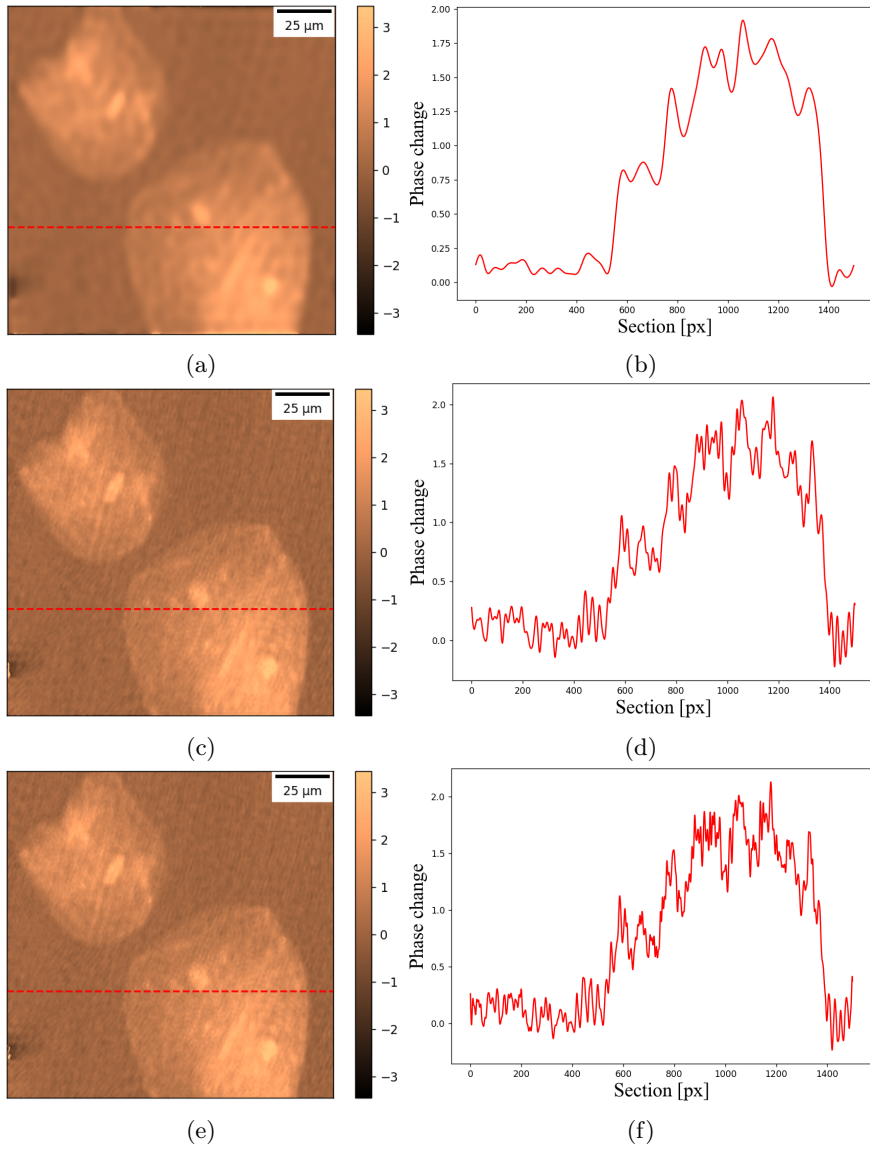
Figure 4.2: The pictures on the left side show phase reconstructions of the same sample with the difference of the magnitude of the cut of the diffraction order. In the pictures on the right, there are shown horizontal sections of these reconstructions displaying the phase change.

During the phase change of the horizontal section, the raised part represents the location of the cell. This allows us to determine the edge between the medium and the cell. We can evaluate the number of pixels (as a measure of image sharpness) needed to move from the sample location without the cell to the location where the cell is already present. This gives an insight into the resolution and sharpness of the reconstruction. The reconstruction sections were taken at the area where the cell wall was as perpendicular to the section.

To assess the resolution, we evaluate the 10-90% width of the steepest slope of the phase profile in the section. The analysis procedure is demonstrated in Fig. 4.3. The place where the global increase occurred was found in the phase profile. The location before the increase was fitted with a horizontal linear line, the same was done for the location after the increase. At the point where these fitted lines intersect the phase profile, the pixel number at which this happened was found, and then the value

$$N_{\mathrm{n,min}} = l_{\mathrm{n}} + 0.1(h_{\mathrm{n}} - l_{\mathrm{n}}), \qquad (4.2)$$

was determined, where l_{n} is the point where the fit intersects the beginning of the increase, h_{n} is the point where the fit intersects the end of the increase, n is the number of sections and $N_{\mathrm{n,min}}$ will represent the point from where we take the minimum of the increase. And then

$$N_{\mathrm{n,max}} = l_{\mathrm{n}} + 0.9(h_{\mathrm{n}} - l_{\mathrm{n}}), \qquad (4.3)$$

where $N_{\mathrm{n,max}}$ represents the point from where we take the maximum value of the increase. According to equations (4.2) and (4.3) we found the lower and the upper limits of the edge. Subtraction of these values gives the number of pixels that represent it.
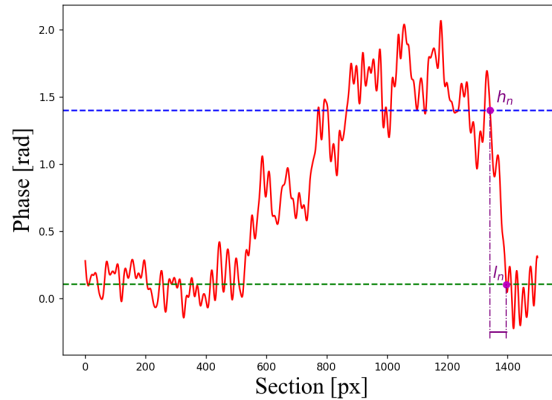

Figure 4.3: An example of a horizontal section with fitted lines. The purple dots show places where the fitted lines intersect the phase profile that we are looking for. The guidelines are there for the visualization of pixel distance representing slope.

From Fig. 4.3 it is visible that for the analysis, it is better to take the decreasing progression of the cell because of the higher slope. Relations (4.2) and (4.3) have been adapted accordingly. This process was repeated for 5 sections that were close to each other. The average value of the number of pixels was

taken as the result. The standard deviation with which this pixel resolution value was determined was also calculated. This was done for reconstructions with different cut radii of the spectrum cut sizes and the dependence of the resolution on this spectrum cut was observed.

The dependence of noise on the spectrum cut was also observed. The magnitude of the noise was determined as the standard deviation at the sample-free area. The statistics were performed in the same way as for the resolution of the image.
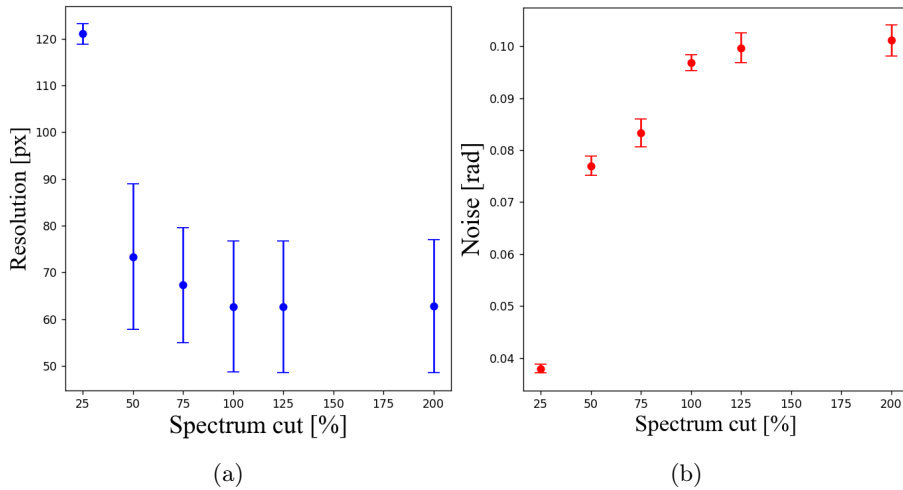

Figure 4.4: Panel (a) shows the dependence of resolution on the size of the spectrum cut. The lower values of the resolution represent more details in the reconstructed phase image. Panel (b) shows the dependence of the noise on the size of the spectrum cut. The spectrum cut is in percentage values, where 100% corresponds to the value of the maximum transmitted spatial frequency obtained from a calculation using Eq. (3.3).

From the plot shown in Fig. 4.4 (a), we can see that the number of pixels that represented the cell edge was significantly higher for the small spectrum cut. By gradually increasing the spectrum cut, the number of these pixels decreased until the value of the maximum transmitted spatial frequency was reached. From this point on, the resolution remained approximately constant. The noise, shown in Fig. 4.4 (b), degrades the quality, and therefore the spectrum cut size is sought where there is some trade-off between resolution and noise. From the results shown, we can confirm that this size is in proximity to the area of the maximum transmitted spatial frequency.

Chapter 5

Design of advanced holographic microscopy

The aim of performing the experiment described in Chapter 3 and the following analysis presented in Chapter 4 was to get the knowledge, gain experience, and prepare for the design of advanced digital holography, which will lead to even more accurate results and offer a greater range of possibilities for cell observation.

A fundamental aspect for achieving better reconstruction of a digital hologram recording is to select the appropriate components and set them to optimally exploit the Fourier domain of the camera. Especially, the position and size of the resulting diffraction orders. With the right orientation and period of the interference fringes, but also with the right choice of lateral optical magnification, the diffraction orders will reach an arrangement where all three orders in the spectrum are still visible in their entirety so that they do not overlap, but at the same time, they reach their largest possible sizes at the camera.

The (0th) diffraction order is twice as large as the (-1st) and ($+1^{st}$) diffraction orders. From Fig. 3.4 and Eq. (3.3) can be seen that it would be sufficient to use a smaller magnification, which would make the diffraction orders larger. We can also see in this spectrum that the diffraction orders are all arranged horizontally next to each other. This configuration with the optimized size of the diffraction orders is shown in Fig. 5.1 (a).

However, if it were possible to somehow shift the (-1st) and ($+1^{st}$) order along the y-axis direction, they would gain more space. This can be achieved by tilting the interference fringes, resulting in a diagonal configuration of the diffraction orders. The Fig. 5.1 (b) shows the ideal diagonal configuration of the diffraction orders. But of course, in reality, it is more profitable to have the diffraction orders a little smaller in size than this case, for the convenience of cutting out ($+1^{st}$) diffraction order from the spectrum. Hence, the calculation has been performed to obtain a limit we cannot exceed. At a smaller magnification, the diffraction orders would overlap, and (-1st) and ($+1^{st}$) would not be visible in their entirety in the Fourier spectrum, making a correct reconstruction impossible at the expense of a larger field of view.

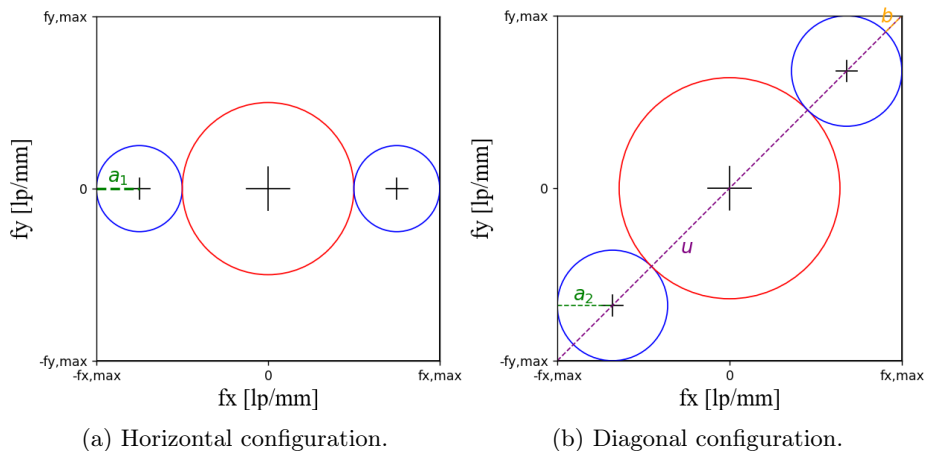(a) Horizontal configuration. (b) Diagonal configuration.

Figure 5.1: Demonstration of the configuration of diffraction orders in the Fourier spectrum. The spectrum is in the image plane.

The calculations started with estimating the Fourier domain, whose size can be determined from equations (2.8) and (2.9). As the camera used in the experiment had square pixels, the Fourier space had the same size in both the x and y directions. Let us start with the calculation of the magnification limit for horizontal configuration. Here, we can express

$$a_1 = \frac{2f_{\mathrm{x,max}}}{8},$$
(5.1)

where a_1 is the radius of the smaller diffraction orders in this type of configuration. Twice the obtained maximum is taken based on the chosen coordinate system. Thanks to this result, we are able to express the boundary condition linking camera parameters, illumination wavelength, and magnification to achieve the configuration shown in Fig. 5.1 (a), and it is given as

$$\frac{\mathrm{NA}}{\beta} \leq \frac{\lambda}{8\Delta x},$$
(5.2)

Now we can start looking into diagonal configuration. Using the Pythagorean theorem, we calculated the diagonal size on which the diffraction orders are located. This diagonal size is made up of their diameters and also the two parts at the corners. This can be given in the equation

$$u = 8a_2 + 2b,$$
(5.3)

where a_2 is the radius of the smaller diffraction orders in diagonal configuration, b is the size of the remaining part of the diagonal at the corner, and u is the size of the space diagonal given as

$$u = 2\sqrt{f_{\mathrm{x,max}}^2 + f_{\mathrm{y,max}}^2}.$$
(5.4)

Using one of the smaller diffraction orders and the Pythagorean theorem, we can express

$$(a_2 + b)^2 = a_2^2 + a_2^2.$$
(5.5)

This gave us a system of two equations with two unknown quantities. Solving them yields the radius of the diffraction orders. The result was substituted into relation (3.3) to couple the radius with the lateral magnification of the imaging optical system. The boundary condition for this configuration can be expressed as

$$\frac{\text{NA}}{\beta} \leq \lambda \sqrt{\frac{1}{\Delta x^2} + \frac{1}{\Delta y^2}} \frac{3\sqrt{2} - 2}{14}. \tag{5.6}$$

Given that for the camera, we used $\Delta x = \Delta y$, the condition could be simplified to

$$\frac{\text{NA}}{\beta} \leq \frac{\lambda}{\Delta x} \frac{3\sqrt{2} - 2}{14}. \tag{5.7}$$

The validity of these conditions was established by substituting the parameters from the conducted experiment and comparing them with the obtained values gained by substituting the a_1 and a_2 values into the Eq. (3.3) for the $\nu'_{\max}$. The results are that for the horizontal configuration shown in Fig. 5.1 (a), it would be possible to get the best size of diffraction orders at the magnification of 22.24 instead of the magnification of 46 used in the described experiment. The centers of the diffraction orders will be for the (-1st) order at [-3a_1,0], for the (1st) order at [3a_1,0] and for the (0th) order at [0,0].

For the diagonal configuration, it was concluded that to get this size of diffraction orders in the experimental setup shown in Fig. 3.1, it would be necessary to achieve a magnification of 17.36. The centers of the diffraction orders will be for the (-1st) order at [-3$\frac{a_2}{\sqrt{2}}$,-3$\frac{a_2}{\sqrt{2}}$], for the (1st) order at [3$\frac{a_2}{\sqrt{2}}$,3$\frac{a_2}{\sqrt{2}}$] and for the (0th) order at [0,0].

It is important to note that equations (5.2) and (5.7) with properly located diffraction orders provide design conditions for a correct complex-amplitude reconstruction. In practice, setting a slightly larger magnification for the fixed wavelength and numerical aperture is beneficial to avoid equalities in equations (5.2) and (5.7), hence, also overlaps in the spectrum.

Chapter 6

Summary an outlook

Digital holographic microscopy is a technique, which allows us to observe living cells in real-time and by capturing images of a hologram on camera. This technique is based on recording and processing the intensity pattern (2.1) originating from interference between the object and the reference wave. Thanks to the numerical reconstruction of these recordings, it is possible to get the depth information of the observed cell. Concerning the geometry of interfering waves, there exist two main approaches of capturing holograms, which were discussed in Chapter 2, in-line and off-axis digital holography.

The purpose of this work was to construct a simple digital holographic microscope in order to understand and approve its basic principles. These were used for analysis and quantification of the single-shot complex-amplitude retrieval. Moreover, the setting and choice of the optical parameters were discussed in order to obtain the optimized holographic performance.

In Chapter 3, there is a detailed description of the constructed experimental setup, which followed the rules of off-axis digital holography using a mirror to create the tilted reference wave. The key components used in this setup are listed in Table 3.1, with all necessary details. We have completed the experiment and as a result, we were able to obtain holographic recordings of samples containing cheek cells. The recorded data was processed using the Python programming language in the JupyterLab interactive development environment to obtain a final reconstruction. This experiment resulted in single-shot phase reconstructions of unstained cheek cells without any internal interference.

Chapter 4 was mostly focused on the quantification of the results obtained from the experimental setup described in the Chapter 3. However, it also describes in detail the experimental trade-offs for the individual properties of the used components. Based on the data we have collected, it can be concluded that the spectral cut size plays a crucial role in the reconstruction process due to the information contained in both high and low spatial frequencies. The plots presented in Fig. 4.4 confirm the validity of the optimal size of the spectral cut, as determined by Eq. (3.3). Increasing the spectral cut beyond this optimal size causes unnecessary noise excess in the reconstruction.

This work made a solid background to start looking at further possibilities for improving the parameters and performance of the holographic microscope. We determined the optimal size of the diffraction orders in the Fourier spectrum in two different configurations. The first was a configuration with horizontally

or vertically oriented interference fringes, which led to the optimal magnification of 22.24 for the microscope objective with NA = 0.4 and wavelength of 633 nm. The second configuration considered diagonally oriented interference fringes. Here, optimal exploitation of the detector was achieved for a lateral magnification of 17.36, while preserving all remaining imaging conditions. These calculations coupled the magnification, numerical aperture of the microscope objective, and used wavelength with parameters of the used camera.

The future design will provide an advanced holographic microscope to observe cells flowing in the microfluidic channel. The method is based on an imaging flow cytometry that examines flowing objects. If the flow velocity is set appropriately, the cells sediment toward the wall of the microfluidic channel while rotating due to a shear flow. The approach allows for the scanning of cells from different angles, thus representing the tomographic measurements. In particular, we will focus on designing a high-resolution holographic microscope that provides the resolution necessary for observing individual cell organelles. Therefore, it is required to achieve superior optical quality over the whole field of view.

Bibliography

[1] G. M. Cooper. *The Cell: A Molecular Approach.* Sunderland (MA): Sinauer Associates, 2nd edition, 2000.

[2] B. Albert, A. Johnson, J. Lewis, D. Morgan, M. Raff, K. Roberts, and P. Walter. *Molecular Biology of Cell.* Garland Science, New York, 5th edition, 2007.

[3] W. Dioni. Eosin as a nuclear stain in botany and as an economical substitute for carmine in zoology. *Miscape*, 2006.

[4] Ch. Holzner, M. Feser, S. Vogt, B. Hornberger ans S. B. Baines, and Ch. Jacobsen. Zernike phase contrast in scanning microscopy with x-rays. *Nature Physics*, 6:883–887, 2010.

[5] M. Shribak, J. LaFountain, D. Biggs, and S. Inouè. Orientation-independent differential interference contrast microscopy and its combination with an orientation-independent polarization system. *J Biomed Opt*, 13(1), 2008.

[6] Ch. Zuo, Q. Chen, and A. Asundi. Transport of intensity equation: a new approach to phase and light field. In *Holography, Diffractive Optics, and Applications VI*, volume 9271, page 92710H. SPIE, 2014.

[7] S. McVitie and D. T. Ngo. Quantitative measurements of phase using the transport of intensity equation. *Journal of Physics*, 126(1):012041, 2008.

[8] Ch. Zuo, J. Sun, J. Li, J. Zhang, A. Asundi, and Q. Chen. High-resolution transport-of-intensity quantitative phase microscopy with annular illumination. *Scientific Reports*, 7, 2017.

[9] A. J. Carroll, G. A. van Riessen, E. Balaur, I. P. Dolbnya, G. N. Tran, and A. G. Peele. Propagation-based x-ray phase contrast imaging using an iterative phase diversity technique. *Journal of Optics*, 20(3):035605, 2018.

[10] V. Arrizon and M. Cruz. Experimental results of phase retrieval with reduced noise using inline digital holography and an iterative method. volume 8011, 2011.

[11] F. Yang, Y. Jiang, Y. Li, X. Pang, Y. Ling, H. Wang, Y. Yang, X. Li, J. Tian, and X. Wang. Cell image reconstruction using digital holography with an improved gs algorithm. *Frontiers in Physiology*, 13:1040777, 2022.

[12] J. Chun, T. A. Zangle, S. Kalim, J. S. Hong, S. E. Pefley, X. Zheng, J. K. Gimzewski, and M. A. Teitell. Rapid, massively parallel single-cell drug response measurements via live cell interferometry. *Biophys J.*, 101(5):1025–31, 2011.

[13] V. Petrov, A. Pogoda, V. Sementin, A. Sevryugin, E. Shalymov, D. Venediktov, and V. Venediktov. Advances in digital holographic interferometry. *Journal of Imaging*, 8(7), 2022.

[14] U. Schnars and W. Juptner. Direct recording of holograms by a ccd target and numerical reconstruction. *Appl. Opt.*, 33:179–181, 1994.

[15] E. N. Leith and J. Upatniek. Reconstructed wavefronts and communication theory. *Journal of the Optical Society of America*, 52:1123–1130, 1962.

[16] D. Gabor. A new microscopic principle. *Nature*, 161:777–778, 1948.

[17] J. Bajer. *Optika 2*. chlup.net, Olomouc, 2018.

[18] Z. Monemhaghdoust, F. Montfort, Y. Emery, Ch. Depeursinge, and Ch. Moser. Off-axis digital holographic camera for quantitative phase microscopy. *Biomed. Opt. Express*, 5(6):1721–1730, 2014.

[19] T. Kreis. *Handbook of Holographic Interferometry - Optical and Digital Methods*. WILEY-VCH Verlag GmbH & Co. KGaA, Weinheim, 2005.

[20] M. K. Kim. *Digital Holographic Microscopy - Principles, Techniques, and Applications*. Springer, New York, 2011.

[21] P. Picart. *New Techniques in Digital Holography*. ISTE Ltd and John Wiley & Sons, Inc., 2015.

[22] B. E. A. Saleh and M. C. Teich. *Fundamentals of Photonics*. John Wiley & Sons, Inc., 3rd edition, 2019.

[23] M. K. Kim. Principles and techniques of digital holographic microscopy. *SPIE Reviews*, 1(1):018005, 2010.

[24] P. Ferraro, A. Wax, and Z. Zalevsky. *Coherent Light Microscopy - Imaging and Quantitative Phase Analysis*. Springer, New York, 2010.